Analyst

PAPER

View Article Online
View Journal | View Issue

Cite this: *Analyst*, 2018, **143**, 5822

Ultrasmall black phosphorus quantum dots: synthesis, characterization, and application in cancer treatment†

Mingqian Wang,[a] Ying Liang,[a] Yajun Liu,[a] Guohong Ren,[a] Zhicheng Zhang,[a] Shishan Wu *[a] and Jian Shen*[a,b]

Black phosphorus quantum dots (BPQDs) are gaining popularity for applications in various fields because of their unique advantages. For biomedical applications, good biosafety is a prerequisite for the use of BPQDs *in vivo*. However, currently, little information is available about their basic properties and biocompatibility, which are of great importance for potential biomedical applications. In this work, we prepared BPQDs by an improved solvothermal method and evaluated their fluorescence, biocompatibility, and photothermal therapy (PTT) effectiveness. First, the structures and functions of the BPQDs were investigated at the cellular and molecular levels. It was found that the fluorescence of the BPQDs is wavelength-dependent and that they absorb in the UV-vis range; also, their quantum yield reached 10.2%. In particular, we considered the morphology and lysis of human red blood cells, *in vivo* blood coagulation, and plasma recalcification profiles. We found that the BPQDs have excellent biocompatibility and hemocompatibility with blood components. Overall, concentrations of the BPQDs $\leq$0.5 mg mL^{-1} had few adverse effects on blood components. The resulting BPQDs can efficiently convert near-infrared (NIR) light into heat; thus, they are suitable as a novel nanotheranostic agent for PTT of cancer. Meanwhile, the results of serum biochemistry tests revealed that the indicators were at similar levels for mice exposed to BPQDs and for control mice. Furthermore, from bio-distribution analysis of the BPQDs, no apparent pathological damage was observed in any organs, especially in the spleen and kidneys, during the 30 day period. Our research indicates that the BPQDs have bio-imaging capability and biocompatibility and highlights their great potential in the therapy of cancer.

Received 20th August 2018,
Accepted 18th September 2018

DOI: 10.1039/c8an01612g

rsc.li/analyst

1. Introduction

Black phosphorus quantum dots (BPQDs) are a new material (generally, their diameters are <10 nm) with photoluminescence behavior; they were first discovered in 2015.[1–3] Currently, BPQDs are attracting extensive attention because of their unique electronic, optical, and structural properties.[4,5] Compared with other materials, such as graphene and MoS$_2$, black phosphorus (BP) exhibits a thickness-dependent band gap that is tunable from about 0.3 eV for bulk to 2.0 eV for single layer and is a highly efficient photosensitizer when applied as a photocatalyst and in energy conversion storage.[6,7] In addition, both BP sheets and BPQDs show broad absorptions across the entire visible light region; thus, they possess near-infrared (NIR) photothermal properties.[2] Compared with other zero-dimensional materials, such as carbon quantum dots and inorganic quantum dots, BPQDs have a much higher surface to volume ratio. Black phosphorus has photodegradable character from elemental to biocompatible phosphorus oxides, broad light absorption, and excellent biocompatibility in living tissues; its puckered lattice configuration can increase its drug loading capacity.

By virtue of its unique advantages, BP has attracted great interest in many fields, such as composites and sensors,[8–11] photodetectors,[12] thin-film solar cells,[13] and anode materials in lithium-ion batteries;[14,15] also, it has been applied with success in the utilization of graphene (analogues or derivatives).[16] However, efficient and reliable strategies for the controllable synthesis of BPQDs are still urgently needed, and the potential biomedical application of these BPQDs should be further explored.

Photothermal therapy (PTT) is considered to be an emerging non-invasive modality for the treatment of various cancers.[17]

---

[a] *School of Chemistry and Chemical Engineering, Nanjing University, 163 Xianlin Avenue, Nanjing, Qixia District, 210023, China. E-mail: shishanwu@nju.edu.cn*

[b] *Jiangsu Collaborative Innovation Center of Biomedical Functional Materials, Jiangsu Key Laboratory of Biomedical Materials, College of Chemistry and Materials Science, Nanjing Normal University, Nanjing, 210023, China*

† Electronic supplementary information (ESI) available. See DOI: 10.1039/c8an01612g

Ideally, PTT reagents absorb excitation light, leading to hyperthermia (>43 °C) and causing photothermal ablation of cancer cells. Recently, contrast agents, which can transform light energy into thermal energy, have been effectively employed in PTT for accurate disease diagnosis and therapy.[18,19] Nanocomposites, especially theranostic nanocomposites, which have combined therapeutic and diagnostic capabilities, have promise for providing new therapeutic strategies in the biomedical field. To date, at least three types of nanophotothermal agents have been extensively developed, including carbon-based nanomaterials of carbon nanotubes (CNTs) and graphene;[20–23] metal nanostructures of Fe nanoparticles (NPs);[24] Co-based nanosheets[25] and Au NPs;[26] and copper chalcogenide semiconductors of CuS and $Cu_{2-x}Se$ NPs.[27,28] Tungsten oxide nanocrystals of $W_{18}O_{49}$ and chemically exfoliated MoS_2 have also been reported to exert photothermal effects under 980 nm and 808 nm laser irradiation, respectively.[29,30] However, these nanomaterials have certain disadvantages in biological and medical applications; their heavy metal compositions (Fe, Co, Au, Cu, W) and inherent toxicities lead to serious side effects.[31] Several *in vitro* and *in vivo* studies have indicated that these nanocomposites (NCs) are intrinsically cytotoxic because they release free radicals of heavy metals from the surface oxidation of NCs into the bloodstream *via* different biochemical pathways. Consequently, sub-cellular aggregation of heavy metals leads to cell death. Additionally, synthesis of NCs has limitations related to the requirement for expensive and toxic chemicals and multistep, time-consuming, and complicated procedures. Moreover, the NCs significantly quench their luminescence by incorporating a magnetic element. Thus, the development of new photothermal agents with good biosafety is still necessary to further improve the therapeutic efficacy of PTT.

BPQDs have great potential as a biomedical reagent.[32,33] In the present work, ultrasmall BPQDs were synthesized by an improved solvothermal method in *N*-methyl-2-pyrrolidone (NMP). We demonstrate that the BPQDs have excellent water dispersibility, high stability (in phosphate-buffered saline (PBS) buffer and NaCl solutions), high quantum yields (QYs), and excellent NIR absorption properties; these properties are promising for fluorescence imaging and PTT. We then investigate the effects of the BPQDs on the structure and function of key blood components: specifically, the morphology of human RBCs, hematolysis and *in vitro* blood coagulation. Furthermore, BPQDs have a strong ability to transform incident 808 nm NIR light into heat energy and ablate cancer cells. As far as we know, this study demonstrates the application of BPQDs for fluorescence and photothermal imaging-guided *in vivo* therapy. This study provides a potential candidate material based on BPQDs for efficient theranostic applications and clinical translation.

2. Experiments

2.1. Materials

BP crystals of high purity were purchased from a commercial supplier (99.998%, Nanjing XF NANO Materials Tech Co., Ltd); NMP (99.5%) and sodium hydroxide (NaOH) were obtained from Aladdin Reagents. 3-(4,5-Dimethylthiazol-2-yl)-2,5-diphenyltetrazolium bromide (MTT) was purchased from Sigma (St Louis, MO, USA). Double-distilled water (18.2 MΩ) was obtained from a Milli-Q system (Millipore, Bedford, MA, USA) and was used in all experiments. The human cervical cancer (HeLa) cells were purchased from the Cell Bank of Culture Collection of Chinese Academy of Sciences (Shanghai, China). Fresh rabbit whole blood was provided by the Jiangsu Blood Center. All the chemicals were used as received without further purification.

2.2. Preparation of the BPQDs

The BP bulk crystals were stored in an Ar glovebox prior to use. The preparation of BPQDs is given in detail as follows. First, BP crystals were ground into a black phosphorus powder and added to a bottle with NMP solution in an Ar environment. Secondly, 20 mg BP powder was added to a bottle with 20 mL NMP solution in a Ar environment. Then, the obtained 20 BP NMP solution, 180 mL of NMP, and 200 mg NaOH were added to a flask and maintained with vigorous stirring for 6 h at 140 °C. The experimental procedure was performed in a nitrogen environment. Afterward, the resulting suspensions were centrifuged for 20 min at 7000 rpm to separate the centrifugate and supernatant. The acquired brown supernatant was the NMP solution of BPQDs. Finally, the BPQDs solution was centrifuged for 20 min at 12 000 rpm, and the precipitate was rinsed repeatedly with water and re-suspended in aqueous solution.

2.3. Characterization of the BPQDs

2.3.1 Characterizations. The morphology of the BPQDs was observed by a high-resolution transmission electron microscope (HRTEM, JEOL-2100F, Japan). The sample for the HRTEM was prepared by dropping the BPQDs aqueous solution onto a copper grid and air drying for 1 h at room temperature. The UV-vis absorption spectrum of the BPQDs aqueous solution was recorded using a UV-2550 spectrophotometer (Shimadzu Corporation, Japan). The fluorescence emission spectra of the BPQDs aqueous solution were recorded on a Hitachi F-7000 fluorescence spectrophotometer (Hitachi High-Technologies Corp., Tokyo, Japan). The UV-visible absorption and fluorescence emission spectra measurements were performed in 1 cm^2 quartz cuvettes at room temperature. The AFM images of the BPQDs were then recorded in tapping mode under air using a Multi-Mode 8 microscope (Bruker) and processed by NanoScope Analysis software. Raman spectroscopy was also performed (Renishaw, RM1000-Invia) in a backscattering configuration excited with visible laser light (wavelength = 514 nm), a notch filter cut-off frequency of 50 cm^{-1}, and a focus spot size of 5 μm. The crystalline structure of the BPQDs was investigated with reference to the X-ray diffraction (XRD; Rigaku RDA-cA X-ray diffractometer, Japan) patterns obtained by passing Cu Kα radiation through a nickel filter. X-ray photoelectron spectroscopy (XPS) analysis was conducted on a PHI 5000 Versa Probe. The fluorescence images of the cells were acquired using a laser scanning confocal microscope (TI-E-A1R, Nikon, Japan). The photoluminescence (PL) lifetime decay profile was measured using a customized confocal microscope setup with a 345 nm pulsed laser for excitation.

2.3.2 Quantum yield measurement. Quantum yield is an important parameter for evaluating the fluorescence strength of BPQDs. Generally, quinine sulfate is used as a reference substance to measure their quantum yields. The specific experimental procedure is as follows: firstly, a small amount of quinine sulfate (Φ = 54%) was dissolved in 0.1 M solution of H_2SO_4, and the BPQDs were dissolved in deionized water. Then, the absorbance values of the BPQDs and quinine sulfate were measured at 360 nm. It was ensured that both of the absorbance values were less than 0.05. In addition, the integral fluorescence intensities of the BPQDs and quinine sulfate were obtained by measuring both their PL emission spectra at an excitation wavelength of 410 nm. Finally, the quantum yield of the BPQDs was calculated using the following equation:

$$\Phi = \Phi_{\text{st}}(K_{\text{x}}/K_{\text{st}})(\eta_{\text{x}}/\eta_{\text{st}})^2$$

where K is the integrated emission of the fluorescence spectrum, η is the refractive index of the solvent and the subscript 'X' denotes the sample. The absorption threshold was set below 0.05 to minimize re-absorption effects. The experimental procedures were performed according to a published paper.[32]

2.4. Effects of BPQDs on the morphology and lysis of red blood cells (RBCs)

2.4.1 RBC morphology. Fresh whole blood was centrifuged at 1000*g* for 5 min, and the supernatant was carefully removed. The RBC pellet was washed with PBS and then incubated for 10 min at room temperature with different concentrations of the BPQDs solution and dissolved in PBS. After that, the RBCs were fixed for 2 h with 4% formaldehyde and subjected to a dehydration gradient with ethanol solutions (75, 85, 95, and 100%, v/v). After air drying, the RBCs were coated with gold and observed with a scanning electron microscope (SEM, Philips XL-30, Holland).

2.4.2 RBC lysis. The RBCs suspension (16% in PBS, v/v, 50 mL) was added to 1 mL of PBS (as a negative control) or different concentrations of the BPQDs solutions dissolved in PBS. As a positive control, 50 μL of the RBCs suspension was added to 1 mL of water to yield complete hemolysis. After incubation for a certain time, the RBCs suspensions were centrifuged at 1000*g* for 5 min, and the supernatants were collected. Then, the absorbance values of the released hemoglobin (Hb) in the supernatants (200 μL) were measured at 540 nm with a microplate reader (Multiskan MK3; Thermo Lab-systems, Finland). The hemolysis in the presence of the BPQDs was calculated by comparing the absorbance values of the tested supernatants to that of the control.

2.5. Effect of BPQDs on *in vitro* blood coagulation

The coagulation assays of the BMS and functionalized BMS were investigated through three tests: activated partial thromboplastin time (APTT), prothrombin time (PT) and thrombin time (TT). Fresh, anticoagulated rabbit blood was centrifuged at 1000*g* for 10 min, and the resulting supernatant (platelet-poor plasma) was collected. The platelet-poor plasma (270 μL) was mixed with BPQDs solutions (30 μL in PBS) at 37 °C for 30 min. After adding the corresponding reagents, all the assays were measured with a Semi-automated Coagulometer (RT-2204C, Rayto, USA).

2.6. Plasma recalciflcation time (PRT) assay

Blood was collected in a sodium-citrate vacutainer and then centrifuged at 3000 rpm at 8 °C for 15 min to obtain the platelet-poor plasma (PPP). One milliliter of PPP at 37 °C was added to a polypropylene tube containing the BPQDs solution and incubated for 1 min. Then, 1 mL of $CaCl_2$ solution with a concentration of 0.025 mol L^{-1} was added. The tubes were shaken in a 37 °C bath, and the process was monitored. The period until the silky fibrin appeared was recorded as the PRT.

2.7. Cytotoxicity assays

2.7.1 MTT experiment. To assess the cytotoxicity of the BPQDs, HeLa cells (5×10^3) were seeded into a 96-well plate overnight before incubation with BPQDs for 48 h. Then, 20 μL of MTT (5 mg ml^{-1}) was added to each well, and the cells were incubated for another 4 h. The medium containing MTT was then discarded, and 150 μL DMSO was added to each well and shaken to dissolve the crystals. Absorbance values were measured at $OD_{490\ \text{nm}}$ with an iMark microplate reader (Bio-Rad). Cell survival rates were calculated according to the following formula:

$$\text{RGR} = [(D_{\text{t}} - D_{\text{b}})/(D_{\text{nc}} - D_{\text{b}})] \times 100\%$$

where D_{t} is the absorbance of the sample; D_{nc} is the negative absorbance in the control group; and D_{b} is the absorbance of the blank control group.[33]

2.7.2 Assay of cell apoptosis and necrosis. To detect cell apoptosis and necrosis, the Annexin V-FITC/PI apoptosis assay (TransGen Biotech) was performed. In brief, HeLa cells at a density of 1.0×10^5 cells per mL were seeded onto a 24-well plate and cultured overnight. Subsequently, the cells were treated with 1 mg mL^{-1} BPQDs samples for 24 h. Finally, the cells were harvested, rinsed thrice with PBS, stained with Annexin V-FITC as well as PI (Annexin V-FITC labels apoptotic cells while PI labels necrotic cells), and analyzed by a Cell Lab Quanta SC flow cytometry system.

2.8. Cell imaging

The HeLa cells (4×10^4 cells per mL) were seeded on sterile WHB coverslips (WHB, China) as well as the bottom of 24-well plates, which were cultured (37 °C, 5% CO_2) overnight. After the cells adhered to the coverslips, the cells were treated with BPQDs dissolved in fetal bovine serum-free DMEM. The cells were then washed three times with fresh phosphate buffered saline (PBS, pH 7.4) and fixed with 4% formaldehyde for 10 min at room temperature. After being washed with PBS, the cells were mounted with glycerol and then observed with a confocal laser scanning microscope.

2.9. Photothermal ablation of cancer cells

To evaluate the PTT therapy potential of the BPQDs, different concentrations of BPQDs solutions were irradiated by 808 nm light with a power density of 1.0 W cm^{-2} for 10 min. The temperature of the BPQDs solution was recorded with an infrared (IR) thermal camera. The photostability of the BPQDs was tested for 5 cycles of irradiating and cooling processes. For photothermal ablation of cancer cells, HeLa cells were incubated with 100 mg mL^{-1} BPQDs solution for 12 h and then irradiated with a laser (808 nm, 1.0 W cm^{-2}) for 10 min. After incubation for another 12 h, MTT assays were used to evaluate the cell viability.

2.10 Tumor model

Female nude mice were purchased from Nanjing Sikerui Biological Technology Co. Ltd and used under protocols approved by the Nanjing University Laboratory Animal Center. 2×10^6 HeLa cells suspended in 50 mL PBS were subcutaneously injected into the right leg of each female nude mouse. The mice bearing HeLa tumors were treated when the tumor volume reached ~100 mm^3.

2.11. *In vivo* photothermal imaging

To test the *in vivo* photothermal imaging of the BPQDs, different concentrations of BPQDs (50 μL) were irradiated by 808 nm light with a power density of 1.0 W cm^{-2} for 5 min. The temperature of the BPQDs solution was recorded with a near infrared (NIR) thermal camera.

2.12. Histological analysis

Healthy female Kunming (KM) mice were purchased from Nanjing Sikerui Biological Technology Co. Ltd. All animal operations were conducted in accordance with the guidelines of the Institutional Animal Care and Use Committee. The material dispersed in PBS (pH 7.4, 0.2 mL) at a total dose of 10 mg kg^{-1} was intravenously injected into the mice *via* the tail vein. KM mice ($n = 3$) who received injections of only physiological saline were chosen as the control group. For serum biochemistry assays, three important indicators for liver functions (alanine aminotransferase (ALT), aspartate aminotransferase (AST), total bilirubin (TBIL)) and two renal function indicators (creatinine (CREA) and blood urea nitrogen (BUN)) were determined. After the blood collection, the mice were sacrificed immediately. The organs (heart, liver, spleen, lung, and kidneys) were removed and fixed in 4% formaldehyde, then dehydrated and embedded in paraffin. 5 mm transverse sections were cut (Leica RM2235 microtome) and stained for histological analysis.

2.13. Statistical analysis

All of the data were expressed as mean ± standard deviations (SD). Each test was repeated three or more times. Analysis of variance (ANOVA) statistical tests were performed, and p values less than 0.05 were considered to be statistically significant.

3. Results and discussion

3.1. Physicochemical characterization of the BPQDs

The ultrasmall BPQDs were prepared on a large scale from black phosphorus (BP) bulk crystal by using an improved solvothermal method.[3] The scheme of the synthesis process is shown in Fig. 1A. In brief, BP crystals were ground and then subjected to continuous ultrasound for 3 hours to form BP sheets. The BP sheets were added to a flask with saturated NaOH NMP solution under vigorous stirring for 6 h at 140 °C in nitrogen atmosphere. During the whole preparation process, all the experiments were carried out in N_2 atmosphere. It is well known that BP is sensitive to water and oxygen and readily oxidized under visible-light irradiation. More details on the synthesis procedure can be found in the Experimental section. Compared with other mechanical and liquid exfoliation methods, this ultrasound and solvothermal synthesis is facile and controllable and enables production of BPQDs on a large scale.

The low magnification transmission electron microscope (TEM) image in Fig. 1B depicts the morphology of the BPQDs with an average size of 2.1 ± 0.1 nm. The (040) and (111) planes of the BPQDs, associated with lattice fringes of 0.261 and 0.254 nm, can be observed in the high-resolution transmission electron microscope (HRTEM) image, as shown in Fig. 1C.[33] The X-ray diffraction (XRD) pattern of the BPQDs (Fig. 1D), revealing reflective patterned peaks of d_{020} = 5.2 Å, d_{040} = 2.6 Å, and d_{060} = 1.7 Å at 2θ = 16.9°, 34.2°, and 52.3°, respectively, indicates the orthorhombic structure of crystalline BP.[34]

As seen from the AFM images, the as-prepared BPQDs exhibit a typical height of 2.0 ± 1.0 nm, suggesting the composition of 1 to 5 ultrathin layers based on one monolayer thickness of 0.53 nm (Fig. 1E). These small and uniform BPQDs are expected to find promising applications in catalysis and photothermal treatment. The AFM image shows the topographic morphology of the BPQDs (Fig. 1E), and the height profile reveals thicknesses of ~0.58 to 1.45 nm (Fig. 1F).[2] Generally, AFM-measured thickness values for monolayer LTMs are slightly higher than the theoretical value due to the substrate roughness. Thus, the AFM results indicate that mono- and double-layer BPQDs have been produced using the improved thermosolvent method. This conclusion is further corroborated by the statistical AFM analysis in Fig. 1E, which shows a relatively narrow size distribution and gives an average thickness of 0.92 ± 0.33 nm.

Raman spectroscopy is an effective technique for sample identification by providing detailed vibrational and rotational modes. Herein, Raman spectra were acquired to study the

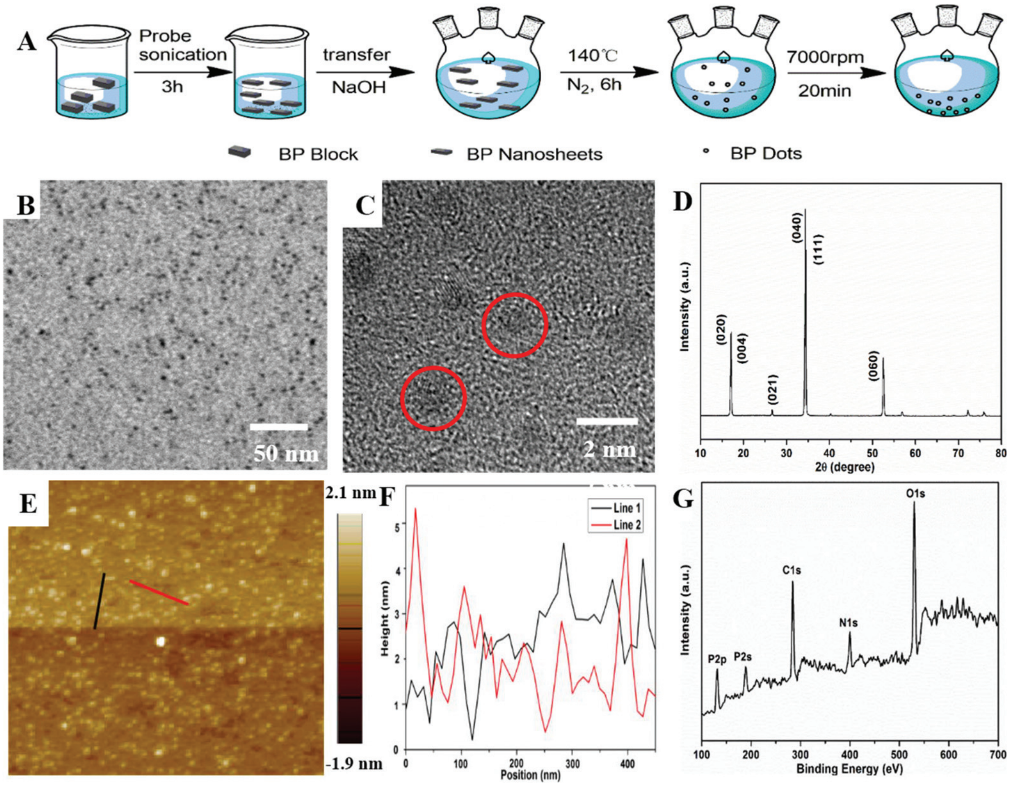

Fig. 1 (A) Schematic of the synthesis process to prepare BPQDs using a solvothermal method in NMP. (B) TEM image of the BPQDs. (C) HR-TEM image of the BPQDs. (D) XRD spectra of the BPQDs. (E) AFM image of the BPQDs. (F) Height profiles along the red and black lines in E. (G) XPS survey of the BPQDs.

structural transformation of BP during the liquid exfoliation process. Fig. S1† shows the Raman spectrum of the BPQDs, which gives three prominent peaks located at 362, 436, and 464 cm^{-1}, corresponding to the A_{1g}, B_{2g}, and A_{2g} modes of orthorhombic crystalline phosphorus. These sharp modes further confirm that the BPQDs disintegrated from bulk BP crystal yet retained their crystalline nature. Compared to the bulk BP, both the B2 g and A2 g modes of the BPQDs are blue-shifted by around 6.8 cm^{-1}, while the A1 g mode is only blue-shifted by 4.2 cm^{-1}; this can be attributed to decreases in the thickness and the lateral dimensions, as found for the BPQDs and for MoS_2 QDs.[35,36] Furthermore, X-ray photoelectron spectroscopy (XPS) was used to analyze the chemical composition of the BPQDs. As shown in Fig. 1G, the XPS survey shows a predominant P 2p peak at around 129.9 eV and an O 1s peak at 532.1 eV. It has been reported that BP is sensitive to water and oxygen and can be degraded to P_xO_y under visible light irradiation.[5] Therefore, the O signal should arise from the oxidation of BP due to exposure of the BP sample to the atmosphere before the XPS measurement. The high-resolution P 2p spectrum shows two peaks at around 130.3 eV and 129.5 eV (Fig. S2†), assignable to the $2p^{1/2}$ and $2p^{3/2}$ binding energies, respectively.[37] A peak in the high energy region (around 133.9 eV) is indicative of the oxidation of the BPQDs.

3.2. Optical properties

As observed for other carbon-based quantum dots, the BPQDs showed excitation-dependent PL under excitation wavelengths from 400 to 600 nm (Fig. 2A). With increasing excitation wavelength, the fluorescence peak red shifted and the peak intensity decreased. Meanwhile, when the excitation wavelength was over 420 nm, the fluorescence emission of the BPQDs was excited dependently. Specifically, this λ_{ex}-dependent PL behavior is useful for multicolor *in vitro* biological imaging applications.

By fitting the fluorescence decay curve with a double-exponential function, a PL lifetime of 4.03 ns was calculated for the BPQDs excited at 355 nm (Fig. 2B). Also, the fluorescence quantum yield upon excitation at 355 nm was calculated to be 10.2% using quinine sulfate as a reference substance. The BPQDs has good light performance, which is derived from intramolecular electronic transitions.

The BPQDs showed excitation and emission peaks at 410 nm and 470 nm, respectively (Fig. 2C). The photographs of BPQDs in aqueous solution displayed bright green fluorescence (inset of Fig. 2C). In addition, the BPQDs showed excitation-dependent PL with emission wavelengths from 400 nm to 570 nm. With excitation wavelengths of 350 to 410 nm, the maximum emission wavelength remained con-

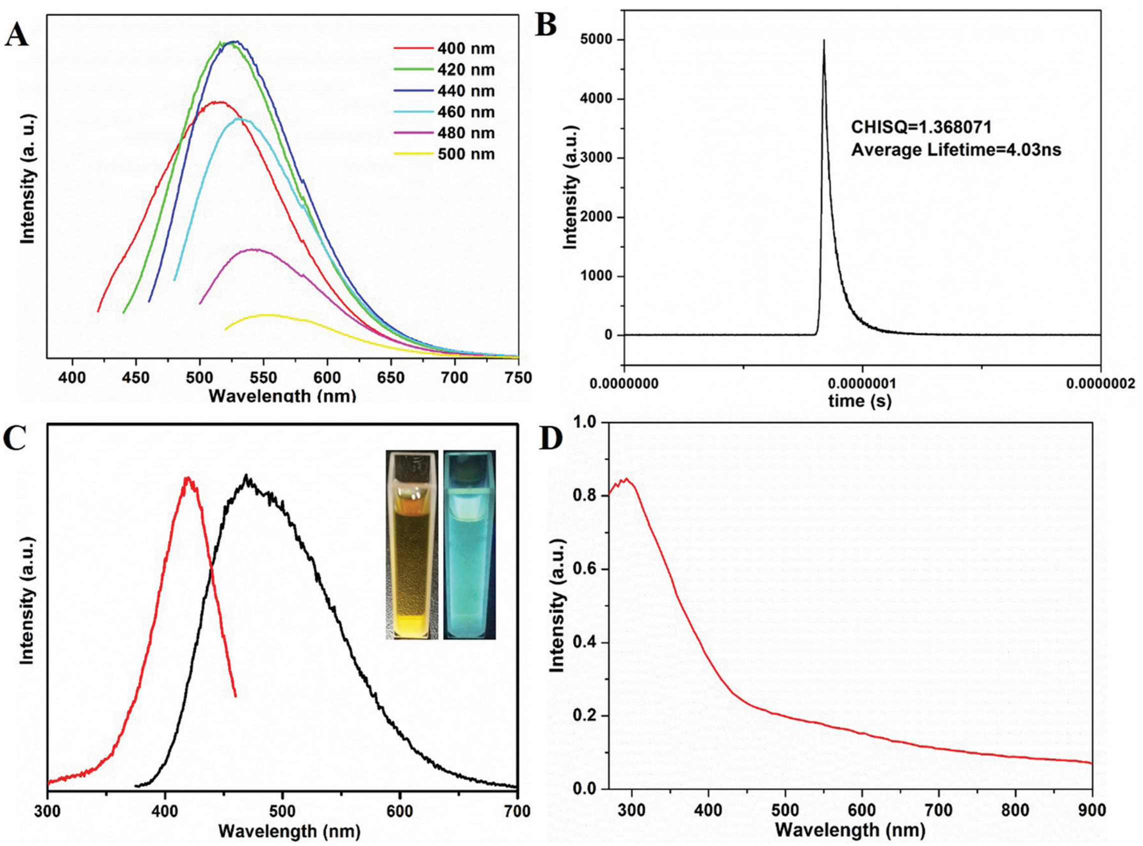

Fig. 2 (A) Excitation-dependent emission spectra of the BPQDs. (B) The fluorescence lifetime of the BPQDs. (C) The maximum excitation and emission wavelengths of the BPQDs. The inset is a photograph of the fluorescence of the BPQDs under UV light illumination (365 nm). (D) The UV-Vis spectrum of the BPQDs.

stant. UV-Vis spectroscopy of the BPQDs was performed; the results exhibited broad absorption in the visible and NIR bands, which is consistent with previous reports and suggests promising potential in photothermal conversion applications.[7] The UV-Vis spectroscopy results of the BPQDs are similar to previous reports, such as small-BP nanosheets,[38] graphene oxide (GO),[39] and WS_2,[40] which exhibit broad absorptions in the visible and NIR bands; this suggests promising potential in photothermal conversion applications (Fig. 2D).

3.3. Effects of BPQDs on morphology and lysis of RBCs

RBCs have been widely used in biosafety evaluations of various biomedical materials. RBCs are responsible for the transport of oxygen and carbon dioxide; they are the most abundant blood cells, comprising 40% to 50% (v/v) of human whole blood. In most cases, blood-contact biomaterials will inevitably interact with RBCs.[41,42] Moreover, because of their high abundance and easy handling, RBCs are a good model for preliminary investigations of the complicated interactions between other mammalian cell membranes and foreign biomaterials. In this work, we studied the effects of BPQDs on the morphology and lysis of RBCs to determine the interaction of BPQDs with the membrane structure of RBCs.

Normally, mature RBCs display the shape of biconcave disks. They are very sensitive to membrane-active substances that interact with the RBC membrane and alter the morphology of the RBCs. Fig. 3A shows RBCs in the presence of different concentrations of the BPQDs. Overall, the BPQDs appear to affect the morphology of the RBCs in a concentration-dependent manner. Specifically, the morphology of the RBCs in 0.1 to 0.5 mg mL^{-1} of the BPQDs did not change compared with the control.

In this work, the morphology of the RBCs was demonstrated by optical images of the negative control, positive control and 0.5 mg mL^{-1} of the BPQDs. The morphology of the RBCs in the presence of the BPQDs did not change compared with the negative controls, even at high concentrations of BPQDs. It is inferred that the BPQDs possess favourable blood compatibility and negligible toxicity with respect to RBCs.

Hemolysis is considered to be a means of evaluating the biocompatibilities of various biomedical materials. Hemolysis causes the release of hemoglobin from RBCs and indicates disturbance of their membrane integrity. A hemolysis value of under 5% is regarded as the benchmark of biosafety for biomedical materials.[43] In this work, Fig. 3B shows the hemolysis percentage of RBCs exposed to different concentrations of the

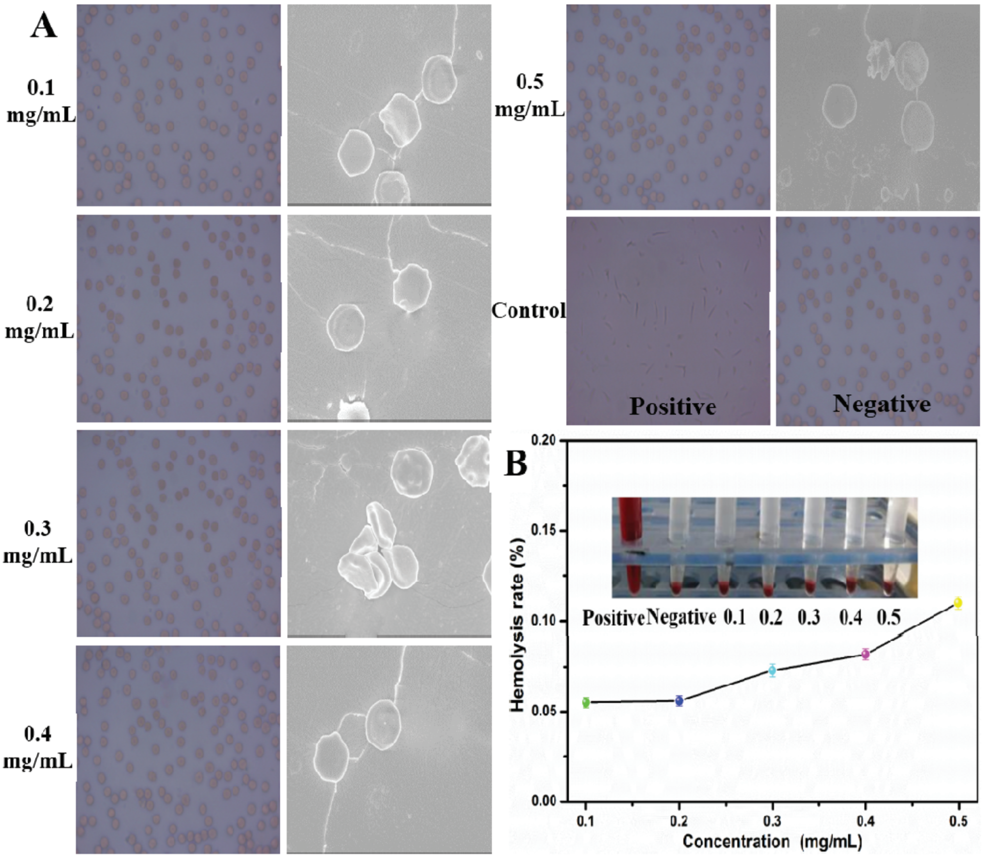

Fig. 3 (A) Optical and SEM images of RBCs treated with different concentrations of BPQDs (0.1, 0.2, 0.3, 0.4, and 0.5 mg mL^{-1}). (B) Hemolysis of RBCs incubated with different concentrations of BPQDs at room temperature.

BPQDs along with incubation times of up to 24 h. From Fig. 3B, RBCs in 0.1 and 0.5 mg mL^{-1} of the BPQDs did not lyse even at an incubation time of 24 h compared to the PBS control. These results indicate that the lysis of RBCs in the presence of BPQDs was dose- and time-dependent. The interaction of BPQDs with the RBC membrane plays a significant role *in vivo* applications.

Blood coagulation is one of the most important functions of blood tissue. Desirable blood coagulation should occur on particular occasions, such as during unexpected bleeding.[44,45] Too weak or too strong blood coagulation ability can have harmful or even lethal outcomes. The individual biofunctions of the components can be weakened or strengthened by the presence of agonists or activators, which can impair normal blood clotting function. Biomaterials that contact blood tissue often act as agonists or activators of the coagulation system by interacting with the coagulation components, possibly causing adverse effects to the host. Hence, the effects of biomaterials on blood coagulation must be evaluated in preclinical tests.

The blood coagulation system includes the intrinsic pathway, the extrinsic pathway, and the common pathway.[46] APTT and PT are mainly used to examine the intrinsic and extrinsic pathways, respectively, whereas TT is a measure of the functional integrity of circulating fibrinogen and thus can be used as an indicator of the common pathway (Fig. S3–S5†). As shown in Fig. S1,† the APTT of the BPQDs was 14.7 ± 0.5 s, which was higher than that (14.4 ± 0.4 s) of normal blood plasma. Meanwhile, there were no significant differences between the other samples and normal blood plasma. On the other hand, the PT and TT measurements indicated that the BPQDs did not affect normal blood plasma. These results show that the BPQDs do not cause intrinsic or extrinsic blood coagulation.

Plasma recalcification profiles are used to mimic the intrinsic coagulation system *in vitro* (Fig. S6†).[47] The intrinsic pathway is initiated when blood comes into contact with a surface, while the extrinsic pathway is initiated upon vascular injury, leading to exposure of tissue factor (TF). Therefore, the longer the PRT for a biomaterial, the better the anticoagulant activity of the biomaterial. Clotting times of recalcified plasma in the presence of different surfaces are presented in Fig. S4.† The BPQDs gave a short clotting time in the recalcified plasma solutions of the negative control, which suggests that the BPQD films can prolong PRT.

3.4. Cytotoxicity assays, hemocompatibility and cell imaging

Before biological application, the cytotoxicity of BPQDs toward HeLa cells was evaluated by the conventional MTT assay. The results showed that after 48 h of incubation with 0.5 mg mL^{-1} BPQDs, the cell viability was still over 92% (Fig. 4A). Because the maximum concentration tested was larger than the necessary quantity and the exposure times were much longer for the bioimaging study, the BPQDs possess low cytotoxicity and can act as an excellent bioimaging reagent.

The cytocompatibility of the BPQDs was further determined by flow cytometry analysis. The results in Fig. 4B illustrate that the rates of cell apoptosis and necrosis did not increase significantly after incubation of HeLa cells with BPQDs with a concentration of 0.5 mg mL^{-1} for 24 h. This proves that the BPQDs have good cytocompatibility.

After incubation with 0.5 mg mL^{-1} BPQDs for 4 h at 37 °C, fluorescence images of the BPQDs-labeled HeLa cells at different excitation wavelengths were acquired by LSCM. It can be clearly observed that the intensity of the green fluorescence which appeared in the BPQDs-treated cells was higher compared to the cells treated without BPQDs after 0.5 h of incubation. The cytoplasm of the HeLa cells clearly showed blue fluorescence at an excitation wavelength of 403 nm (Fig. 4C). However, the nuclei of the HeLa cells did not show any fluorescence, suggesting that either the BPQDs did not migrate into the nuclei at all or the fluorescence was completely quenched by the nuclei. Quenching by the nuclei is highly unlikely; hence, this result suggests that the BPQDs have a much higher binding affinity to the cytoplasm than to the nuclei. To further confirm the localization of the BPQDs inside the cells, we stained the cell nuclei with DAPI (Fig. 4E, blue channel). We observed that the BPQDs were preferentially located in the cytoplasm and nucleolus (Fig. 4F, overlay) as detected by LSCM. The uptake of the BPQDs by HeLa cells may be similar to the pathways of some CDs, which penetrate into the cell membrane by disturbing the structure and conformation of the lipid bilayer. The attractive fluorescence and extraordinary biocompatibility of the BPQDs are highly appropriate for biomedical applications, especially fluorescence imaging of cell labeling and fluorescent tracing of drug delivery.

3.5. *In vitro* cell experiments and *in vivo* photothermal imaging

The BPQDs were investigated as a photothermal agent for *in vitro* cancer cell ablation under laser irradiation. After incubation with the BPQDs solutions for 4 h, the HeLa cells were irradiated with an 808 nm laser (1.0 W cm^{-2}) for 4 min. Staining the cells with a Live–Dead Cell Staining Kit further demonstrated the excellent photothermal therapy efficacy of the BPQDs. All cells were dead (indicated by red color) and no living cells (indicated by green color) were found after the cells were incubated with 100 ppm BPQDs and exposed to 808 nm laser irradiation (Fig. 5A). When the power intensity was maintained at 1.0 W cm^{-2} and the time was increased to 4 min, most of the cancer cells were killed with a solution of 0.1 mg mL^{-1} BPQDs. Thus, a dose-dependent PTT effect can be observed. In contrast, only a few cells died when they were not incubated with BPQDs solutions. Next, we investigated the BPQDs as a photothermal agent for *in vitro* cancer cell ablation under laser irradiation. It should be noted that the photothermal ablation efficacy was dependent on the concentration of BP nanoparticles (Fig. 5B). The results demonstrate good PTT efficiency of the BPQDs in sterilizing cancer cells.

To monitor the *in vivo* photothermal effects of the BPQDs, the changes in temperature in the tumor area were recorded using a thermal imaging apparatus. It should be noted that the accumulation of the BPQDs in the tumor through the enhanced permeability retention (EPR) effect after intravenous injection was not sufficient for photothermal therapy of the tumor. Tumor-bearing mice were intratumorally injected with BPQDs solution (0.2 mL, 0.5 mg mL^{-1}), and exposed to

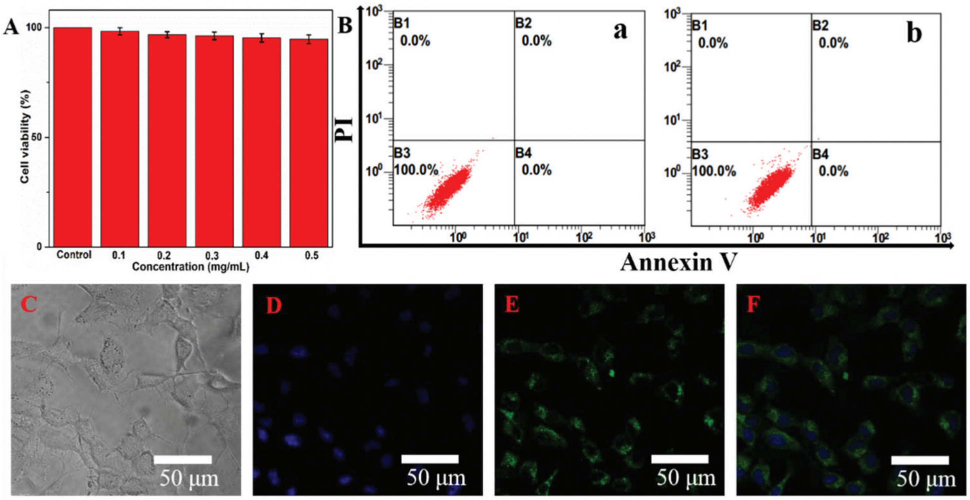

Fig. 4 (A) The proliferation rate of HeLa cells incubated in BPQDs for over 48 h with different concentrations. (B) Flow cytometry analysis of HeLa cells after incubation with 100 μg mL^{-1} of BPQDs for 24 h: (a) control group and (b) BPQDs group. (C–F) Confocal images of HeLa cells observed under blue, green, and overlay channels. The cells were incubated with 0.5 mg mL^{-1} BPQDs medium for 3 h and the cell nuclei were stained using DAPI. All the scale bars are 50 μm.

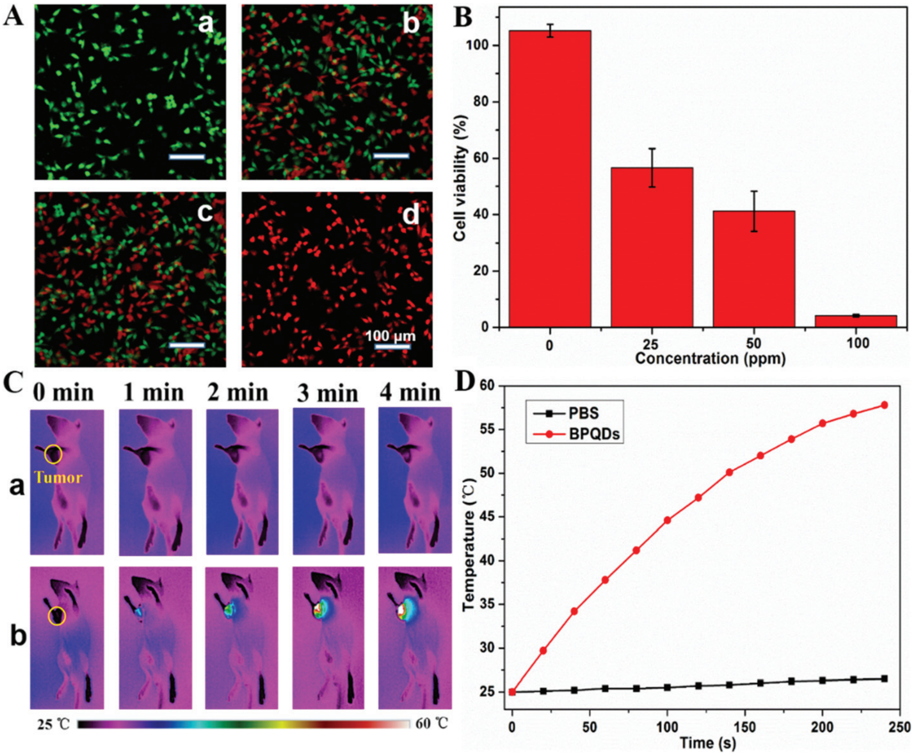

Fig. 5 (A) Comparison of the photothermal destruction of HeLa cancer cells upon addition of BPQDs ((a) 0, (b) 25, (c) 50, and (d) 100 ppm) and irradiation with an 808 nm laser at 1.0 W cm^{-2}, 4 min. Fluorescence images of cells stained with calcein AM (live cells, green fluorescence) and PI (dead cells, red fluorescence). (B) Relative viabilities of HeLa cells after the various treatments (n = 4). (C) Thermal images of mice bearing HeLa tumors after injection of phosphate buffered saline (PBS) solutions (a) and BPQDs solutions (b). (D) Tumor temperature changes of mice bearing HeLa tumors during laser irradiation as indicated in (a).

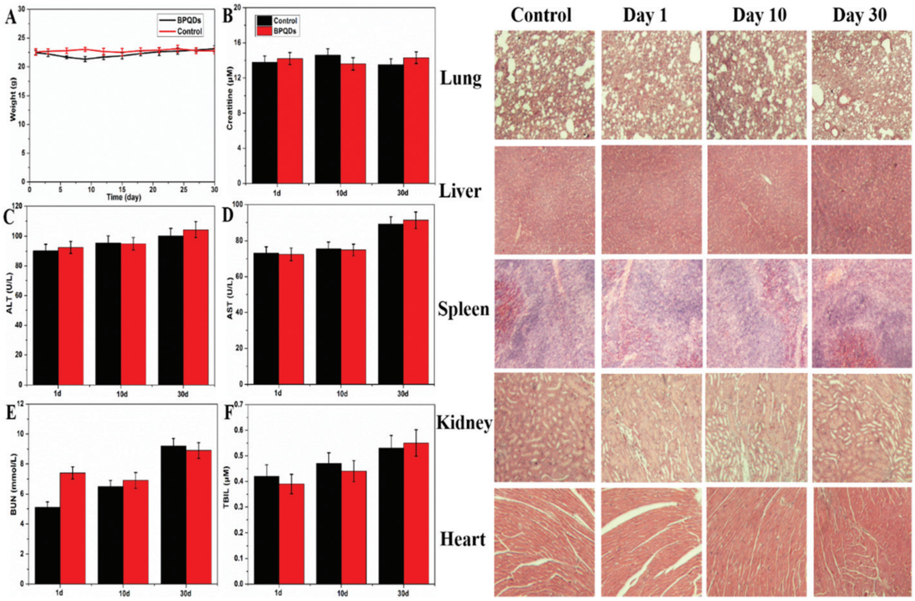

Fig. 6 (A) Body weights of the BPQDs-treated mice during 30 days. (B–F) Blood biochemistry analysis of the BPQDs-treated mice. The indicators include CREA, ALT, AST, DUN, and TBIL. All data were collected at 1, 10, and 30 days after intraperitoneal injection. (G) Pathological evaluation (hematoxylin and eosin stained images) of tissues obtained from the lung, liver, spleen, kidney, and heart of BPQDs-treated mice at 1, 10, and 30 days postinjection.

808 nm laser light with a power density of 2.0 W cm^{-2}. Under irradiation, the temperature of the tumor increased significantly from 25 °C to 57 °C within 4 min (Fig. 5C and D). In comparison, the temperature of the tumors without injection of BPQDs only slightly increased by 5 °C under the same irradiation conditions. These results demonstrate that the BPQDs can serve as a PTT agent for photothermal ablation of tumors.

3.10 Weight, excretion, biodistribution, and pathological evaluation

The body weights and behaviors of the treated mice were monitored on a daily basis to evaluate the *in vivo* toxicity of the BPQDs. Treatment with the BPQDs did not induce any visible adverse reactions on the behaviors of the mice during 30 days, while the body weights of the treated mice decreased slightly after 2 days (Fig. 6A). After that, the body weights of the mice began to recover gradually until the 14th day and reached control levels. For further medical applications, pharmacokinetics and biosafety are the two most important characteristics to be taken into consideration.

Meanwhile, serum biochemistry tests were also performed for quantitative evaluation of three important hepatic indicators (alanine aminotransferase (ALT), aspartate aminotransferase (AST), and total bilirubin (TBIL)) and two indicators for kidney functions (creatinine and blood urea nitrogen (BUN)).[48] We tested these markers because creatinine, ALT, AST, TBIL, and BUN have close correlations to the functions of the liver and kidneys of mice. CREA, ALT, AST, TBIL, and BUN did not show statistical differences between untreated and treated mice (Fig. 6B–D). After 30 days, all the biochemical parameters of the mice treated with BPQDs were thoroughly restored to normal. This indicates that the administration of BPQDs does not cause apparent damage to the organs of mice. Taken together, the preliminary results of the *in vivo* toxicity studies reveal that the BPQDs have good biocompatibility.

To further evaluate the therapeutic efficacy and the *in vivo* toxicity of the BPQDs, major organs of the mice were sliced and stained with hematoxylin and eosin (H&E) for histology analysis. The pathological figures of the major organs were demonstrated by histology at 1, 10, and 30 days. From Fig. 6G, it can be seen that the organs of the mice in the control group remained stable, especially the liver and lungs, compared with the healthy mice during the entire time period.

4. Conclusion

In summary, water-soluble and biocompatible BPQDs were prepared in high yield by an improved solvothermal technique. The resulting BPQDs have a uniform size distribution and exhibit excellent biocompatibility and conversion of NIR light into heat; thus, they are suitable as a novel nanotherapeutic agent for photothermal therapy of cancer. We found that the BPQDs, at concentrations of ≤0.5 mg mL^{-1}, neither altered the morphology of RBCs nor caused RBC lysis. Both the *in vitro* and *in vivo* results demonstrate the great potential of the BPQDs in PTT. Also, the BPQDs can be excreted from the liver and kidneys. The tumors of tumor-bearing mice were curbed effectively after photothermal treatment using BPQDs as a heat mediator. Our research highlights the great potential of BPQDs in nano-biomedicine.

Conflicts of interest

There are no conflicts to declare.

Acknowledgements

This work was supported by the Foundation of Jiangsu Collaborative Innovation Center of Biomedical Functional Materials.

References

1 X. Zhang, H. M. Xie, Z. D. Liu, C. L. Tan, Z. M. Luo, H. Li, J. D. Lin, L. Q. Sun, W. Chen, Z. C. Xu, L. H. Xie, W. Huang and H. Zhang, *Angew. Chem., Int. Ed.*, 2015, **54**, 3653–3657.

2 Z. B. Sun, H. H. Xie, S. Y. Tang, X. F. Yu, Z. N. Guo, J. D. Shao, H. Zhang, H. Huang, H. Y. Wang and P. K. Chu, *Angew. Chem., Int. Ed.*, 2015, **127**, 11688–11692.

3 Y. H. Xu, Z. T. Wang, Z. N. Guo, H. Huang, Q. L. Xiao, H. Zhang and X. F. Yu, *Adv. Opt. Mater.*, 2016, **4**, 1223–1229.

4 A. H. Woomer, T. W. Farnsworth, J. Hu, R. A. Wells, C. L. Donley and S. C. Warren, *ACS Nano*, 2015, **9**, 8869–8884.

5 Y. W. Wang, S. Liu, B. W. Zeng, H. Huang, J. Xiao, J. B. Li, M. Q. Long, S. Xiao, X. F. Yu, Y. L. Gao and J. He, *Nanoscale*, 2017, **14**, 4683–4690.

6 Y. Zhang, Y. Zheng, K. Rui, H. H. Hng, *et al.*, 2D Black phosphorus for energy storage and thermoelectric applications, *Small*, 2017, **13**(28), 1700661.

7 Y. Xue, Q. Zhang, T. Zhang, *et al.*, Black phosphorus: properties, synthesis, and applications in energy conversion and storage, *ChemNanoMat*, 2017, **3**(6), 352–361.

8 J. Miao, L. Cai, S. Zhang, *et al.*, Air-Stable humidity sensor using few-layer black phosphorus, *ACS Appl. Mater. Interfaces*, 2017, **9**(11), 10019–10026.

9 C. Zhu, F. Xu, L. Zhang, *et al.*, Ultrafast preparation of black phosphorus quantum dots for efficient humidity sensing, *Chemistry*, 2016, **22**(22), 7357–7362.

10 W. Gu, Y. Yan, X. Pei, *et al.*, Fluorescent black phosphorus quantum dots as label-free sensing probes for evaluation of acetylcholinesterase activity, *Sens. Actuators, B*, 2017, **250**, 601–607.

11 C. Xing, G. Jing, X. Liang, *et al.*, Graphene oxide/black phosphorus nanoflake aerogels with robust thermo-stability and significantly enhanced photothermal properties in air, *Nanoscale*, 2017, **9**(24), 8096–8101.

12 M. Zhu, Y. Osakada, S. Kim, *et al.*, Black phosphorus: a promising two dimensional visible and near-infrared-activated photocatalyst for hydrogen evolution, *Appl. Catal., B*, 2017, **217**, 285–292.

13 X. Ren, J. Zhou, X. Qi, *et al.*, Few-layer black phosphorus nanosheets as electrocatalysts for highly efficient oxygen evolution reaction, *Adv. Energy Mater.*, 2017, **7**(19), 1700396.

14 C. Hao, B. Yang, F. Wen, *et al.*, Flexible all-solid-state supercapacitors based on liquid-exfoliated black-phosphorus nanoflakes, *Adv. Mater.*, 2016, **28**(16), 3194–3201.

15 G. L. Xu, Z. Chen, G. M. Zhong, *et al.*, Nanostructured black phosphorus/ketjenblack-multiwalled carbon nanotubes composite as high performance anode material for sodium-Ion batteries, *Nano Lett.*, 2016, **16**(6), 3955–3965.

16 H. Liu, Y. Zou, L. Tao, *et al.*, Sandwiched thin-film anode of chemically bonded black phosphorus/graphene hybrid for lithium-Ion battery, *Small*, 2017, **13**(33), 1700758.

17 K. Yang, S. Zhang, G. Zhang, *et al.*, Graphene in mice: ultrahigh in vivo tumor uptake and efficient photothermal therapy, *Nano Lett.*, 2010, **10**(9), 3318–3323.

18 S. Lal, S. E. Clare and N. J. Halas, Nanoshell-enabled photothermal cancer therapy: impending clinical impact, *Acc. Chem. Res.*, 2008, **41**(12), 1842–1851.

19 P. K. Jain, X. Huang, I. H. El-Sayed, *et al.*, Noble metals on the nanoscale: optical and photothermal properties and some applications in imaging, sensing, biology, and medicine, *Acc. Chem. Res.*, 2008, **41**(12), 1578–1586.

20 M. Zhang, W. Wang, F. Wu, *et al.*, Magnetic and fluorescent carbon nanotubes for dual modal imaging and photothermal and chemo-therapy of cancer cells in living mice, *Carbon*, 2017, **123**, 70–83.

21 M. Zhang, W. T. Wang, Y. J. Cui, *et al.*, Magnetofluorescent carbon quantum dot decorated multiwalled carbon nanotubes for dual-modal targeted Imaging in chemo-photothermal synergistic therapy, *ACS Biomater. Sci. Eng.*, 2018, **4**(1), 151–162.

22 M. Guo, J. Huang, Y. Deng, *et al.*, pH-Responsive cyanine-grafted graphene oxide for fluorescence resonance energy transfer-enhanced photothermal therapy, *Adv. Funct. Mater.*, 2015, **25**(1), 59–67.

23 G. Gollavelli and Y. C. Ling, Magnetic and fluorescent graphene for dual modal imaging and single light induced photothermal and photodynamic therapy of cancer cells, *Biomaterials*, 2014, **35**(15), 4499–4507.

24 M. Zhang, J. Wang, W. Wang, *et al.* Magnetofluorescent photothermal micelles packaged with GdN@CQDs as photothermal and chemical dual-modal therapeutic agents, *Chem. Eng. J.*, 2017, **330**(15), 442–452.

25 H. Wang, Y. Yuan, Y. Chai, *et al.* Sandwiched electrochemiluminescent peptide biosensor for the detection of prognostic Indicator in early-stage cancer based on hollow, magnetic, and self-enhanced nanosheets, *Small*, 2015, **11**(30), 3703–3709.

26 D. Yang, A. Gulzar, G. Yang, *et al.*, Au nanoclusters sensitized black TiO_{2-x} nanotubes for enhanced photodynamic therapy driven by near-Infrared light, *Small*, 2017, **13**(48), 1703007.

27 C. Zhang, Y. Y. Fu, X. Zhang, *et al.*, BSA-directed synthesis of CuS nanoparticles as a biocompatible photothermal agent for tumor ablation *in vivo*, *Dalton Trans.*, 2015, **44**(29), 13112–13118.

28 S. B. Maddinedi, Green synthesis of Au-Cu_{2-x}Se heterodimer nanoparticles and their in-vitro cytotoxicity, photothermal assay, *Environ. Toxicol. Pharmacol.*, 2017, **29**(59), 29–33.

29 Z. Chen, Q. Wang, H. Wang, *et al.*, Ultrathin PEGylated $W_{18}O_{49}$ nanowires as a new 980 nm-laser-driven photothermal agent for efficient ablation of cancer cells *in vivo*, *Adv. Mater.*, 2013, **25**(14), 2095–2100.

30 B. Liu, C. Li, G. Chen, *et al.*, Synthesis and optimization of MoS_2@Fe_3O_4-ICG/Pt(IV) nanoflowers for MR/IR/PA bioimaging and combined PTT/PDT/Chemotherapy triggered by 808 nm laser, *Adv. Sci.*, 2017, **4**(8), 1600540.

31 G. Wei, Y. Yan, C. Zhang, *et al.* One-step synthesis of water-soluble MoS_2 quantum dots via a hydrothermal method as a fluorescent probe for hyaluronidase detection, *ACS Appl. Mater. Interfaces*, 2016, **8**(18), 11272–11281.

32 M. Zhang, C. Chi, P. Yuan, *et al.*, A hydrothermal route to multicolor luminescent carbon dots from adenosine disodium triphosphate for bioimaging, *Mater. Sci. Eng., C*, 2017, **76**(1), 1146–1153.

33 S. T. Han, L. Hu, X. Wang, *et al.*, Black phosphorus quantum dots with tunable memory properties and multilevel resistive switching characteristics, *Adv. Sci.*, 2017, **4**(8), 1600435.

34 Q. Jiang, L. Xu, N. Chen, *et al.*, Facile synthesis of black phosphorus: an efficient electrocatalyst for the oxygen evolving reaction, *Angew. Chem., Int. Ed.*, 2016, **55**(44), 13849–13853.

35 C. Sun, L. Wen, J. Zeng, *et al.*, One-pot solventless preparation of PEGylated black phosphorus nanoparticles for photoacoustic imaging and photothermal therapy of cancer, *Biomaterials*, 2016, **128**(44), 14053–14057.

36 C. C. Mayorga-Martinez, Z. Sofer and M. Pumera, Layered black phosphorus as a selective vapor sensor, *Angew. Chem., Int. Ed.*, 2015, **127**(48), 14525–14528.

37 J. O. Island, G. A. Steele, H. S. J. van der Zant, *et al.*, Environmental instability of few-layer black phosphorus, *2D Mater.*, 2015, **2**(1), 011002.

38 W. Tao, X. Zhu, X. Yu, *et al.*, Black Phosphorus nanosheets as a robust delivery platform for cancer theranostics, *Adv. Mater.*, 2017, **29**(1), 1603276.

39 L. F. Gao, J. Y. Xu, Z. Y. Zhu, *et al.*, Small molecule-assisted fabrication of black phosphorus quantum dots with a broadband nonlinear optical response, *Nanoscale*, 2016, **8**(33), 15132–15136.

40 L. Cheng, C. Yuan, S. Shen, *et al.*, Bottom-Up synthesis of metal-Ion-doped WS_2 nanoflakes for cancer theranostics, *ACS Nano*, 2015, **9**(11), 11090–11101.

41 S. Li, Z. Guo, Y. Zhang, *et al.*, Blood compatibility evaluations of fluorescent carbon dots, *ACS Appl. Mater. Interfaces*, 2015, **7**(34), 19153–19162.

42 N. N. Reddy, K. Varaprasad, S. Ravindra, *et al.*, Evaluation of blood compatibility and drug release studies of gelatin based magnetic hydrogel nanocomposites, *Colloids Surf., A*, 2011, **385**(1), 20–27.

43 Y. Su, M. Zhang, N. Zhou, *et al.*, Preparation of fluorescent N,P-doped carbon dots derived from adenosine 5′-monophosphate for use in multicolor bioimaging of adenocarcinomic human alveolar basal epithelial cells, *Microchim. Acta*, 2017, **184**(3), 699–706.

44 Z. Liu, Y. Jiao, T. Wang, *et al.*, Interactions between solubilized polymer molecules and blood components, *J. Controlled Release*, 2012, **160**(1), 14–24.

45 Y. Huang, M. Shaw, M. Warmin, *et al.*, Blood compatibility of heparin-inspired, lactose containing, polyureas depends on the chemistry of the polymer backbone, *Polym. Chem.*, 2016, **7**(23), 3897–3905.

46 X. Mu, J. Wang, X. Bai, *et al.*, Black phosphorus quantum dots Induced oxidative stress and toxicity in living cell and mice, *ACS Appl. Mater. Interfaces*, 2017, **9**(24), 20399–20409.

47 X. Wang, X. Chen, L. Xing, *et al.*, Blood compatibility of a new zwitterionic bare metal stent with hyperbranched polymer brushes, *J. Mater. Chem. B*, 2013, **1**(38), 5036–5044.

48 H. Wu, H. Shi, H. Zhang, *et al.*, Prostate stem cell antigen antibody-conjugated multiwalled carbon nanotubes for targeted ultrasound imaging and drug delivery, *Biomaterials*, 2014, **35**(20), 5369–5380.